Thermal and topographic tests of Europa chaos formation models from Galileo E15 observations

F. Nimmo

Dept. Earth and Space Sciences, UCLA, 595 Charles Young Drive E, Los Angeles, CA 90095-1567, USA (nimmo@ess.ucla.edu)

B. Giese

DLR, Rutherfordstrasse 2, 12489 Berlin, Germany (bernd.giese@dlr.de)

Number of pages: 37

Number of figures: 8

Number of tables: 0

Running head: Tests of Europa chaos formation models

Corresponding author:

Francis Nimmo

Dept. Earth and Space Sciences

UCLA

595 Charles Young Drive E

Los Angeles

CA 90095-1567

USA

tel. 310-206-7383

fax. 310-825-2779

Abstract

Stereo topography of an area near Tyre impact crater, Europa, reveals chaos regions characterized by marginal cliffs and domical topography, rising to 100-200 m above the background plains. The regions contain blocks which have both rotated and tilted. We tested two models of chaos formation: a hybrid diapir model, in which chaos topography is caused by thermal or compositional buoyancy, and block motion occurs due to the presence of near-surface (1-3 km) melt; and a melt-through model, in which chaos regions are caused by melting and refreezing of the ice shell. None of the hybrid diapir models tested generate any melt within 1-3 km of the surface, owing to the low surface temperature. A model of the refreezing following melt-through gives effective elastic thicknesses and ice shell thicknesses of 0.1-0.3 km and 0.5-2 km, respectively. However, for such low shell thicknesses the refreezing model requires implausibly large lateral density contrasts (50-100 kg m^{-3}) to explain the elevation of the centres of the chaos regions. Although a global equilibrium ice shell thickness of $\approx$2 km is possible if Europa's mantle resembles that of Io, it is unclear whether local melt-through events are energetically possible. Thus, neither of the models tested here gives a completely satisfactory explanation for the formation of chaos regions. We suggest that surface extrusion of warm ice may be an important component of chaos terrain formation, and demonstrate that such extrusion is possible for likely ice parameters.

Keywords: Europa, Satellites of Jupiter, ices, geophysics, tectonics

1 Introduction

An important discovery of the Galileo spacecraft mission was the existence of areas of chaotic terrain on the surface of Europa (Carr et al. 1998). These areas consist of fractured blocks of pre-existing surface material, surrounded by matrix material and often having sharp, cliff-like margins (see Fig. 1a). The blocks are commonly high-standing relative to the surrounding matrix material, by $\sim$100 m in the case of Conamara Chaos (Williams and Greeley 1998). The mixture of matrix and pre-existing blocks varies from one chaos region to another, as does the size of the regions. Conamara Chaos is an area roughly 100 km across, while patches of chaotic terrain have also been identified in the interiors of 10 km scale lenticulae (Spaun et al. 1998, Greenberg et al. 2003). The pre-existing blocks in Conamara appear to have both moved laterally, without leaving any obvious sign of their motion in the surrounding matrix, and to have tilted sideways (Spaun et al. 1998, Carr et al. 1998).

The importance of chaos terrain is that it potentially provides clues to the nature of Europa's ice shell, in particular its thickness (Carr et al. 1998, Greenberg et al. 1999, Schenk and Pappalardo 2004), subsurface composition and temperature structure. Unfortunately, there is as yet no consensus as to what the existence of chaotic terrain implies. Although the block topography and apparent motion in Conamara Chaos are very suggestive of a "melt-through" event (Carr et al. 1998, Greenberg et al. 1999), in which liquid water reached the surface of Europa, this hypothesis has been challenged (e.g. Collins et al. 2000), mainly because of the enormous power required to cause such an event.

Various aspects of chaos formation have been investigated recently. Pappalardo et al. (1998) suggested a solid-state diapirism mechanism for chaos formation, and both Wang and Stevenson

(2000) and Sotin et al. (2002) argued that enhanced tidal dissipation within the diapir might lead to increased thermal buoyancy and melting. Such solid-state diapir models suffer from the high rigidity and viscosity of the near-surface ice, which makes deformation of the near-surface difficult (Showman and Han 2004). Thomson and Delaney (2001) suggested melt-through caused by focused upwelling plumes driven by seafloor magmatic activity. However, Goodman et al. (2004) have argued that such plumes are likely to be both too broad and too diffuse to account for observed chaos characteristics. Melosh et al. (2004) also argued for melt-through events, adopting a different model for ocean stratification. The consequences of flow in the lower shell during a putative melt-through event have been investigated by Buck et al. (2002) and O'Brien et al. (2002), although the conclusions of the latter may not be correct (see Appendix in Goodman et al. 2004).

An important contribution by Collins et al. (2000) applied simple quantitative tests to some of the hypotheses for chaos formation. These authors concluded that the energy requirements for a melt-through model were difficult to satisfy. However, they recognized that solid-state diapirism was inconsistent with the observed size range of chaos blocks: the model predicts an absence of large (>1 km), elevated blocks, in contradiction to the observations. Collins et al. (2000) proposed an intermediate or hybrid model, similar to that of Head and Pappalardo (1999), in which diapirism gave rise to shallow melting of salt-rich ices.

Here we adopt a similar approach to Collins et al. (2000), in that we develop simple quantitative models of chaos formation. We focus on two aspects: firstly, the thermal conditions required to satisfy the hybrid diapir model; and secondly, the topographic consequences of both the melt-through and the diapir models. A recent survey of chaos topography has been undertaken by Schenk and Pappalardo (2004). Our topographic data are obtained from one area only, but the results should be applicable to other chaos areas which share the same basic features (discussed below). We caution that it is not yet clear whether all chaos terrains are formed in the same fashion.

In Section 2 we discuss the observations of our study area, and in particular the topography. We then proceed to examine two models of chaos terrain formation and topography: the hybrid diapir model (Section 3); and melt-through (Section 4). In Section 5 we discuss the relative merits of the different hypotheses, and make suggestions for further work.

2 Observations

Fig. 1a shows a high-resolution mosaic of Galileo images of an area SE of Tyre impact crater **Fig. 1** obtained during the E15 encounter (see Kadel et al. (2000) for a geological description). The area is dominated by cross-cutting ridges, but also contains several areas of chaos. The largest (CH2) is an irregularly-bordered area at the bottom (north) of the image, containing several large blocks. There is also a 10 km wide lobate area (CH1) at the top (south) of the image, consisting almost entirely of matrix material, referred to by Schenk and Pappalardo (2004) as a lenticula and mapped by Kadel et al. (2000) as knobbly chaos. A final area of chaos (CH3) truncates the prominent diagonally-trending double ridge towards the top of the image. Small pit-like features in the image are secondary impact craters from Tyre.

Fig. 1b shows stereo-derived topography for the area shown in 1a, and profiles across the region are shown in Fig. 2. Only the first two chaos regions referred to above are covered by the stereo data. **Fig. 2** The stereo technique is described in Giese et al. (1998); the horizontal resolution of the topographic model is 200-400 m and the vertical accuracy is generally better than 10 m. An independent stereo model of the same region has recently been published by Schenk and Pappalardo (2004). The two models are in remarkably good agreement, although the Schenk and Pappalardo (2004) model has slightly fewer gaps which allows identification of subtle features, such as a possible trough at the western margin of CH1, not identifiable in our model.

Region CH2 has a complex short-wavelength topographic signature, visible in both Fig. 1b and profiles 12-14 in Fig. 2. The east (left-hand) side of the region has a distinct cliff visible in both the image and the topography, with the background material $\sim$100 m higher than the matrix. Several chaos blocks are clearly elevated with respect to the surroundings by similar amounts; one large block (at the N end of profile 13) appears to have rotated by about 30° and also to have tilted slightly. The overall topography of this region is domical, and rises by 100-200 m above the base of the cliff.

The second chaos region (CH1) is simpler. Again, there is a pronounced cliff at the margins of the matrix material (profiles 2-5), and again the centre of the region is domical and elevated by 100-200 m with respect to the background plains. The margins of the region contain lobate material with lineations suggestive of some kind of extrusion or flow. The sinuous nature of the profiles outboard of the region is not noise, but is a result of crossing numerous ridges. The western edge of the CH1 region is not obvious in the topography (profiles 7-9). The western topography appears to remain elevated beyond the edge of the mapped chaos region, as also noted by Schenk and Pappalardo (2004); a similar effect for region CH2 is also seen in profile 13.

To isolate the shape of the trough at the eastern edge of the CH1 region, profiles 1-6 were aligned on this marginal trough; the result of stacking these profiles is also shown in Fig. 2. Both the marginal trough and the elevated centre are apparent. Although the outboard material slopes downwards towards the chaos region, this result may be an artefact caused by the elevated terrain at the ends of profiles 2-4.

In summary, the chaos regions described here are frequently characterized by a cliff-like marginal trough, which often sharply truncates pre-existing features, and a domically uplifted centre. In particular, the centres of the regions are elevated by 100-200 m with respect to the background plains. In some cases, the elevated area extends beyond the edge of the chaos terrain. Similar features are evident at the much larger chaos feature termed Murias Chaos (see Figueredo et al. 2002). The short-wavelength ($\sim$ 1km) topography of the Conamara Chaos region is complicated, but cliff-like margins and domical uplift are again evident (Schenk and Pappalardo 2004). While it is not clear that all chaos regions share similar characteristics, it is the characteristics outlined above that we will focus on in the models below.

3 Diapirism

The observed chaos morphology and the likelihood of ice shell convection prompted a class of models (e.g. Pappalardo et al. 1998, Spaun et al. 1999) in which chaos regions are formed by the ascent of solid-state diapirs. The existence of such diapirs is widely accepted on the basis of theoretical arguments (e.g. Pappalardo et al. 1998, Rathbun et al. 1998, McKinnon 1999) and the existence of surface features termed pits, spots or domes (Pappalardo et al. 1998, Spaun et al. 1999, Greenberg et al. 2003). The relationship between these latter features and chaos regions is presently unclear (Greenberg et al. 2003).

A disadvantage of the rising diapir model is that it is hard to account for the observed lateral and rotational motion of ice blocks in areas like Conamara Chaos (Collins et al. 2000). These authors therefore proposed a modification to the original hypothesis, similar to that of Head and Pappalardo (1999), in which the rising diapir melts overlying ice which is contaminated with salts. This near-surface, interstitial partial melt allows the surface ice blocks to detach and move as required.

Fig. 3 is a cartoon of the fundamental processes likely to occur. The rising diapir is assumed to be thermally buoyant, though compositional buoyancy may also play a role (Pappalardo and Barr 2004). The buoyant diapir will rise until either the overlying ice is sufficiently cold and rigid to prevent further movement, or the level of neutral buoyancy is reached. Once the diapir stalls it will begin to propagate laterally. As it does so it will cool conductively, warming the surrounding material. If this material is contaminated with salts (e.g. Kargel et al. 2000, Zolotov and Shock 2001, Fanale et al. 2001), it will contain low-melting-temperature components, which will melt to form a brine. Since the centre of the diapir is likely to be closest to the surface, there will be a tendency for this melt to drain laterally; being denser than the surrounding ice, it will also move downwards. Although the diapir is likely to be crack-free due to its relatively high temperature, the surrounding material is probably fractured, permitting fluid flow. The removal of the melt will create subsidence at the surface, as occurs with caldera collapses on Earth. As with calderas, the margin of the collapse feature can be quite sharp. Moreover, the production of melt may allow detachment faulting and sliding of blocks to occur (Head and Pappalardo 1999). Although the topography due to the thermal buoyancy of the diapir will decay with time, any compositional variations will induce permanent uplift (Nimmo et al. 2003a, Pappalardo and Barr 2004). This uplift will be modified by the rigidity of the overlying ice and may therefore extend for a greater lateral distance than the collapse feature. This hybrid mechanism can thus in principle explain the main features of the chaos terrains described. **Fig. 3**

The original analysis of Collins et al. (2000) estimated a melt volume of the order of 1% of the volume of the diapir, but did not include any predictions of the depth at which melting was required to match the observations. As will be seen below, it is this melting depth which provides the strongest constraint on plausible diapir models. Some chaos blocks are no more than 1 km in width (Collins et al. 2000, Fig 1). The ratio of width:depth for the rotating ice blocks is unlikely to greatly exceed 1, implying that partial melt must extend to within a few (≈1-3) km of the surface if detachment faulting along zones of melting is to occur. Two other weaker constraints may also be applied. Firstly, if the marginal subsidence of the matrix relative to the background material is a result of melting, as suggested by Fig. 3, then the integrated thickness of melt generated must be of the same order as the observed subsidence, that is ∼100 m. Secondly, the partially molten zone must persist for long enough to allow detachment and block rotation to take place.

Below, we will apply a quantitative analysis to the two main processes in this model. Firstly, we will examine the depths at which melt can be generated, and the rate at which it is removed. Secondly, we will investigate the likely topography created. We will conclude that even in extremely favourable circumstances, the generation of melt at sufficiently shallow depths (1-3 km) to match the constraints is highly unlikely.

Before embarking on a detailed model description, consideration of some simple physics will illustrate the basic difficulty of generating diapir-induced melting at shallow depths. If a hot body (temperature T_1) is placed in contact with colder background material (temperature T_0), then in the absence of internal heating the initial temperature at the interface is $(T_1 + T_0)/2$ (e.g. Turcotte and Schubert 2002), and this interface temperature will subsequently decrease with time. As explained below, a lower bound on the melting temperature of salty ice is ≈210 K; assuming a diapir temperature of 250 K, the minimum temperature of the surroundings required to generate even infinitesimal melting is 170 K, or about 40% of the depth to the base of the ice shell. Generating melt at shallow depths is exceedingly difficult, simply because the surrounding material is so cold.

3.1 Melting Model

We adopt a simplified 2D Cartesian representation of the situation shown in Fig. 3. The diapir is modelled as a stationary rectangular block of thickness s with its top at depth t below the surface, and having a maximum initial temperature, tapered to the margins, of T_i. The near-surface (salty) ice above a particular depth is assumed to have a melting temperature of T_m, while ice in the diapir or below this depth has a melting temperature of T_b. The ice is otherwise assumed to have uniform thermal properties, with the exception of thermal conductivity (see below). The shell thickness is t_c and the bottom temperature is maintained at a constant value T_b. Since the conductive heat flux through an ice shell as thin as 1 km is still $\approx 10^2$ times smaller than the incident solar radiation, likely variations in subsurface heat flux will not have any appreciable affect on the surface temperature T_s, which we therefore assume constant. The initial thermal state is conductive everywhere except within the diapir. Since the diapir is assumed to be stationary (an assumption discussed in Section 3.4), it is equivalent to an intrusive sill, and the two terms will henceforth be used interchangeably.

Near-surface ice on Europa is cold, heavily fractured, and may contain substantial porosity (Nimmo et al. 2003a). Such porosity will significantly reduce the thermal conductivity, and will increase temperatures at depth, making melting more likely. Similar low thermal conductivity layers have been proposed in the past (e.g. Squyres et al. 1983, Fanale et al. 1990). Alternatively, the ice conductivity may be low because of the presence of clathrate hydrates (e.g. Prieto-Ballesteros et al. 2004) or salts (e.g. Prieto-Ballesteros and Kargel, in press). For instance, pure methane clathrate has a thermal conductivity a factor of $\approx$7 lower than water ice (Ross and Kargel 1998). We will assume an exponentially varying near-surface conductivity $k'(z)$ of the form

$$k'(z) = k - \Delta k \exp(-z/\delta) \tag{1}$$

where z is positive downwards, k is the conductivity at depth, $\Delta k = k - k_s$, where k_s is the surface conductivity and δ is a decay length.

For a given heat flux F the steady-state temperature structure $T(z)$ is given by

$$T = \frac{F\delta}{k} \ln \left[\frac{k - \Delta k \exp(-z/\delta)}{k - \Delta k} \right] + \frac{Fz}{k} + T_s \tag{2}$$

At depths $\gg \delta$, the effect of the reduced near-surface conductivity is to increase the temperature relative to the constant-conductivity case by

$$\Delta T = \frac{F\delta}{k} \ln \left[\frac{k}{k_s} \right] = \frac{(T_b - T_s)\delta}{t_c} \ln \left[\frac{k}{k_s} \right] \tag{3}$$

where T_b, T_s and t_c are defined above. This equation illustrates the fact that increasing δ or decreasing k_s increases the effect of the near-surface layer, as expected. As discussed below, likely values of k/k_s and δ/t_c are 20 and 0.1, respectively. Under these circumstances, at depths $\gg \delta$ the temperature increase is 30% of the total temperature contrast $(T_b - T_s)$, a significant effect. Note that for a conductive shell, the effect of adding such a low-conductivity layer is to reduce the equilibrium shell thickness.

The background initial temperature in our model is given by eq. (2). The subsequent thermal evolution of the system is solved using the finite-difference approach of McKenzie and Nimmo (1999). This approach is described in more detail in the Appendix. The clean ice is assumed never to melt; to avoid numerical instabilities, melting of the salty ice occurs over a temperature range ΔT_m (usually set to 10 K), with the melt fraction increasing from 0 to 100% in a linear fashion over this range. Note that this method is likely to overestimate the amount of melt generated: in reality, a larger rise in temperature is likely required to generate additional melt as the low melting temperature components are removed. Furthermore, melt drainage is likely to occur on timescales short compared to the rate at which melting proceeds (see Section 3.2). In general, grid points did not suffer complete melting; the melt thicknesses given below were calculated by vertically integrating the melt fraction with depth.

The following parameters were adopted for the ice: heat capacity 2100 J kg^{-1} K^{-1}, asymptotic thermal conductivity $k = 3$ W m^{-1} K^{-1}, density 900 kg m^{-3} and latent heat 0.33 MJ kg^{-1}. The brine produced had an assumed density of 1000 kg m^{-3} and a heat capacity of 4200 J kg^{-1} K^{-1}. We adopted a 25 km thick ice shell, since this is roughly consistent with the existence of convection, at least for Newtonian behaviour (e.g. McKinnon 1999) and examined the effect of varying this parameter below. Based on Galileo photopolarimeter-radiometer results (Spencer et al. 1999), the surface conductivity k_s was fixed at 0.15 W m^{-1} K^{-1}. The thickness of the low-conductivity layer is poorly constrained. Theoretical models suggest that it is unlikely to exceed one-quarter to one-third of the conductive shell thickness (Nimmo et al. 2003a), while observations of isolated chaos blocks (e.g. Collins et al. 2000, Fig. 2d) suggest relatively cohesive near-surface material. We adopted a nominal value for δ of 3 km and investigated variations in this quantity below. The lowest likely melting temperature for salty ice is 210 K (Carlson et al. 1999, Kargel et al. 2000) and this value was adopted to maximize the amount of melt generated. The initial temperature of the diapir T_i was set at 250 K, in agreement with convection calculations (McKinnon 1999, Nimmo and Manga 2002), and the surface and bottom temperatures T_s and T_b fixed at 110 K and 260 K, respectively.

Fig. 4a plots a typical model run, at the point when the maximum amount of melt has been produced. In this model, the salty ice extends half-way down the side of the diapir. However, melting only occurs above the diapir, and decreases with lateral distance from the diapir centre. The total amount of melting is small, as expected from the simple physical argument given above. Despite the low ice melting temperature assumed, the mean thickness of brine generated above the diapir is only 30 m, and the maximum melting fraction is 30% . More importantly, the zone of **Fig. 4** melting is confined to an area immediately above the diapir, deeper than 7 km. The same diapir emplaced at shallower levels in the shell generates no melting, because of the buffering effect of the (fixed) surface temperature. Fig. 4b plots the time variation of a vertical temperature profile through the centre of the diapir. The effect of the near-surface low conductivity layer is evident. The temperatures adjacent to the diapir never exceed half the initial temperature contrast, as expected. The timescale for the diapir to cool to the background temperature is determined mainly by its initial thickness.

Fig. 5 plots the sensitivity of the maximum integrated thickness of brine produced to variations in sill depth, thickness and δ. Fig. 5a shows that increasing the depth to the top of the sill increases the amount of melt produced, because the overlying ice is closer to its melting point. However, the most important result is that in no case is melt generated within 5 km of the surface. Increasing the sill thickness increases the total amount of melt produced (Fig. 5b), because more energy is available, and also prolongs the production of melt. Decreasing δ or increasing the melting temperature T_m reduces the amount of brine generated. **Fig. 5**

An additional source of energy available to generate melt is tidal dissipation. Tobie et al. (2003) suggest that tidal dissipation may be concentrated in warm upwelling areas, and that for equatorial areas the maximum tidal heat generation is 2×10^{-6} W m^{-3}. The dashed lines in Fig. 5a show the effect of adding a constant heating term of 2×10^{-6} W m^{-3} within the diapir, and demonstrate that the effect is small.

For all the models examined, the thickness of the partially molten layer never exceeded 1 km, and the depth to the top of this layer always exceeded 90% of the depth to the top of the sill. Thus, as Fig. 5a demonstrates, melting never occurs within about 5 km of the surface for the range of parameters explored. For $\delta \leq$5 km, melt thicknesses >100 m are only obtained for sills at depths

>8 km, and even in these cases, no melt is generated at depths < 7 km.

To examine the robustness of these results further, we investigated the circumstances under which a diapir emplaced with its top at 3 km depth generated any melt. Melt generation required a surface thermal conductivity $k_s \leq 0.005$ W m^{-1}K^{-1}, a decay length δ >35 km or a melting temperature $T_m \leq$195 K. The available constraints, discussed above, make such parameter values highly implausible.

We also varied the shell thickness t_c from its nominal value of 25 km. Increasing t_c results in colder material at the same depth, and thus makes near-surface melting even less likely; decreasing t_c allows warmer material nearer the surface. Shells of 20 km and 15 km thickness, respectively, generate melt with diapirs emplaced at depths $\geq$ 5 km and 3.5 km, respectively, for the nominal parameters. However, a 15 km thick shell is unlikely to undergo thermal convection (McKinnon 1999). We therefore conclude that the diapir mechanism is unable to generate melt within 3 km of the surface for any likely combination of parameters.

3.2 Melt Drainage Timescales

The compaction timescale for melt has been derived by McKenzie (1989) and was previously applied to problems on Europa by Gaidos and Nimmo (2000). The timescale τ is given by

$$\tau = \frac{C h_m \eta}{a^2 \phi^{n-1} \Delta\rho g} \tag{4}$$

where h_m is the thickness of partially molten material, a is the grain size, ϕ is the melt fraction, $\Delta\rho$ is the density contrast between melt and matrix and g is the acceleration due to gravity. For melt fractions >3%, C=100 and n=3 (McKenzie 1989). At low melt fractions, separation only occurs if the dihedral angle between melt and matrix is < 60°. Experiments on pure water ice suggest that this criterion is usually satisfied (Mader 1992).

Assuming a brine viscosity of 10^{-3} Pa s, a layer thickness of 1 km, a grain size of 1 mm, $\Delta\rho = 100$ kg m^{-3} and a melt fraction of 10%, the compaction timescale is O(1 year). The largest uncertainty in this estimate comes from the grain size. However, to increase the drainage timescale to be comparable to the cooling timescale of the diapir ($\sim$100 kyr) requires a grain size $< 5\mu$m. While such small grain sizes cannot be ruled out entirely, they are orders of magnitude smaller than typical terrestrial ice grain sizes of 1-10 mm (Budd and Jacka 1989).

Thus, melt drainage is probably a rapid process compared to the rate at which melt is produced. Hence, at any time, the melt fraction present is likely to be significantly smaller than the maximum melt fractions obtained in Section 3.1; however, the period over which melt fractions are present will be controlled by the diffusion timescale (typically thousands of years). The survival time of the partially molten zone is therefore sufficient to allow gravitationally-induced sliding of chaos blocks (Head and Pappalardo 1999) to occur.

3.3 Uplift

The transient thermal uplift due to the diapir depends on the temperature contrast between itself and the surrounding terrain, the thermal expansivity of ice, and its thickness. As long as the rigidity of the ice is not too large, the thermal uplift is typically O(100 m) and decays with a timescale set by the thickness of the diapir.

The permanent, compositional uplift depends on the buoyancy of the diapir relative to the surrounding, salty ice. Section 3.1 demonstrated that the amount of melting generated by a stationary diapir is small, and unlikely to affect the overall density structure. Neglecting rigidity, the compositional uplift u is given by

$$u = \frac{\Delta\rho}{\rho}\Delta s \tag{5}$$

where $\Delta\rho$ is now the density contrast between clean and dirty ice, ρ is the (dirty) ice density and Δs is the distance that the diapir has penetrated into dirty ice. It is assumed that there is no compositional density contrast between the diapir and the underlying clean ice.

The degree to which the subsurface ice of Europa is contaminated with salts or silicates is essentially unknown. However, the fact that eruption of liquid water to the surface seems to be a rare occurrence suggests that the bulk crustal density does not exceed that of water, ≈ 1000 kg m^{-3}. Thus, the maximum likely density contrast between clean and dirty ice is ≈ 100 kg m^{-3}, and in practice $\Delta\rho$ is probably smaller. For the sake of argument, if $\Delta\rho$ is 50 kg m^{-3} then to produce 100 m of uplift requires a diapir to penetrate 1.8 km into dirty ice. Since chaos regions on Europa commonly exceed 10 km in diameter, such a penetration distance is not unreasonable. This distance also places a lower limit on the thickness of contaminated ice, but since convection is typically associated with ice thicknesses in excess of 20 km, this limit is not very restrictive.

The amount of uplift will be affected by the rigidity of the overlying ice. Assuming an axisymmetric load, we can calculate the resulting uplift as a function of ice rigidity as follows. The subsurface load (due to thermal and/or compositional buoyancy) is expressed as a sum of Bessel functions. This approach is the axisymmetric equivalent to taking the fourier transform, and is described in more detail in Barnett et al. (2002). The deflection of the ice depends on the load dimensions and magnitude, the ice density and the effective elastic thickness of the ice T_e.

Fig. 6 shows the topography generated by an axisymmetric subsurface load of width 10 km, **Fig. 6**
cosine tapered over the outer 20%. The magnitude of the load is equivalent to a density contrast of

45 kg m^{-3} extending over a vertical distance of 1.8 km. Here we assume an ice density of 900kg m^{-3}, a Young's modulus and Poisson's ratio of 1 GPa and 0.3 respectively, an acceleration due to gravity of 1.3 m s^{-2}, and use the first 50 Bessel functions. For low elastic thicknesses, the topography is essentially isostatic. However, as T_e increases, the maximum amplitude of the topography decreases, and the lateral extent of the uplift increases. Estimates of T_e on Europa vary over a rather wide range: studies of Murias Chaos (Figueredo et al. 2002) and a plateau near Cilix impact crater (Nimmo et al. 2003b) yield values of 4-6 km, while studies of double ridges (e.g. Billings and Kattenhorn 2002, Hurford et al. 2004) and dome-like features (Williams and Greeley 1998) yield values of order 0.1 km. Fig. 6 shows that for relatively narrow features, a value of T_e in excess of 1 km is likely to generate an area of uplift significantly wider than the underlying load.

3.4 Comparison with Observations

Several aspects of the hybrid diapir model are consistent with our calculations. The positive topography observed in the chaos region in Figs. 1 and 2 can be accounted for by a diapir with a reasonable density contrast. Furthermore, topographic uplift extending beyond the edge of the chaos region can be explained for reasonable shell elastic thicknesses (Section 3.3).

The principal problem with the hybrid diapir model is the extreme difficulty in generating melt at shallow depths (Section 3.1). While some melt can be generated at depth (Fig. 5), none of the models are capable of generating melt at 1-3 km depth. This inability to reproduce the inferred melting depths is a significant shortcoming of the hybrid diapir model. We note that the convective models of Tobie et al. (2003) also fail to generate any melt within a few km of the surface.

The degradation process responsible for the formation of matrix material is not understood.

However, the modelling of Section 3.1 shows that diapiric activity increases the near-surface heat flux by a factor of at most 2-3. Since the background subsurface heat flux is at least 10^2 times smaller than the incident solar flux, such variations are unlikely to have any appreciable effect on surface temperature. Thus, diapirism will not generate any kind of enhanced surface sublimation. The brine remobilization model of Head and Pappalardo (1999) suffers from the same problem as the hybrid diapir model described above: shallow melt production is simply not possible for reasonable parameter choices.

One possible explanation for the surface degradation is that heating could potentially cause a clathrate hydrate to decompose, liberating vapour which would generated both the inferred volume loss and the degradation. However, at least for CO_2 and methane clathrates, the temperatures required to cause such decomposition are comparable to that required to generate liquid water (Ross and Kargel 1998). While these hydrates therefore suffer from the problems discussed above of generating sufficiently high temperatures, it is possible that similar species undergoing decomposition at lower temperatures could be responsible for the surface degradation.

The model shown in Fig. 4 is a simplification of reality in that it does not include vertical motion of the diapir. However, such vertical motion is actually very unlikely in the shallow subsurface: the ice is probably too cold and rigid to permit upwards motion. One possibility is that plastic yielding and/or brittle deformation might allow the diapir to ascend closer to the surface than in the usual stagnant lid models (Tobie et al. 2004, Showman and Han 2004). Even if such vertical motion does occur, it would have to take place in a time short compared to the conductive timescale of the overlying layer in order for melt generation to occur at shallow levels. It is not yet clear whether this condition is likely to be satisfied.

Thus, although the diapir model contains some attractive features, the production of melt at sufficiently shallow depths to match the hybrid diapir model of Collins et al. (2000) does not appear possible. Either some fundamental process is missing from the model outlined above, or diapirism cannot be the sole explanation for chaos formation.

4 Melt-through Model

Early observations of chaos terrain suggested that they might be the outcome of "melt-through" events in which liquid water reached the surface and then re-froze (Carr et al. 1998, Greenberg et al. 1999). As discussed in Section 1, while this hypothesis apparently explained several observations of chaos regions, its great disadvantage is that prodigious amounts of energy are required to generate such an event (Collins et al. 2000).

Melt-through events are more plausible if the ice shell is initially thin (1-2 km). Such a global ice shell thickness is in fact possible if Europa's mantle resembles that of Io (Greenberg et al. 2002). The canonical value for Io's global heat flux based on ground-based observations is 2.5 W m^{-2} (Veeder et al. 1994), although more recent observations suggest a value closer to 0.2 W m^{-2} (De Pater et al., 2004). Assuming that the Love numbers and dissipation factors Q of the two bodies were identical, then Europa's surface heat flux would be approximately 9% of Io's (e.g. Murray and Dermott 1999). Using the higher estimate of Io's heat flux, Europa's mantle heat flux would be 220 mW m^{-2}, resulting in a conductive ice shell thickness of 2 km. It is not unreasonable that Europa's mantle should be in an Io-like state: as noted by Peale et al. (1979), tidal heating within a silicate mantle leads to a reduction in viscosity, a decrease in Q, and an increase in tidal heating; this positive feedback results in an extensively molten mantle and an Io-like dissipation rate. Unfortunately, inferring the state of the mantle from surface observations is very difficult; nor do models or observations of orbital evolution yet place constraints on the Q of Europa. Thus, the existence of a globally thin ice shell cannot be ruled out on energetic grounds alone.

However, irrespective of the initial shell thickness, any source of heat internal to the shell is unlikely to result in complete melt-through, simply because as the shell thins, conductive heat removal becomes increasingly effective. This is essentially the same effect which makes melt generation so difficult at shallow depths in Section 3.1. O'Brien et al. (2002) did obtain a melt-through event, but only because their model failed to adequately resolve the thickness of the conductive shell (see Goodman et al. 2004). The most likely mechanism for generating melt-through is some kind of local heat pulse supplied by the underlying ocean (Melosh et al. 2004, Thomson and Delaney 2001); however, it is unclear whether either the energetic requirements or the observed lengthscales of chaos regions can be reproduced by such models (Goodman et al. 2004).

In view of the large uncertainties involved, we will not discuss the energetic difficulties of the melt-through model further. Instead, we will focus on the extent to which the observations of the E15 chaos region are compatiable with likely consequences of the melt-through model.

Fig. 7 shows a schematic of the sequence of events. If a melt-through event occurs (Fig. 7a), the initial level of water is at a distance d below the surface of the ice, where **Fig. 7**

$$d = \frac{t_c(\rho_w - \rho)}{\rho_w} \tag{6}$$

where t_c is the ice thickness and ρ and ρ_w are the densities of ice and water, respectively. This vertical offset has been used in the past to infer an ice shell thickness of 0.5-2 km in chaos regions (e.g. Williams and Greeley 1998), and by this hypothesis is responsible for the marginal cliffs observed (Section 2).

The exposed water will freeze rapidly, beginning at the edges (Fig. 7b). A major assumption here is that this freezing ice is effectively welded to the neighbouring unmelted ice. We also assume that lateral shell thickness contrasts can persist over the refreezing timescale. Such contrasts will be removed by lateral flow in the lower portion of the ice shell; however, for the shell thicknesses of a few km which we derive below, the rate of lateral flow is sufficiently slow that it can be neglected (Buck et al. 2002, O'Brien et al. 2002, Nimmo 2004).

As the refreezing ice thickens, it will experience an upwards force proportional to its thickness due to Archimedes' principle. Normally this upwards force would result in upwards motion (isostatic uplift) of the thickening ice, but in this case the ice is assumed to be pinned at the edges. The result (c.f. Allison and Clifford 1987) is an inverted bowl-shaped profile, similar to that observed (Fig. 7c).

To quantify this effect, we assume that the ice has a flexural rigidity D. The resulting effective elastic thickness T_e of the ice is given by

$$D = \frac{ET_e^3}{12(1-\sigma^2)} \tag{7}$$

where E is the Young's modulus and σ is the Poisson's ratio. For a Cartesian case, the upwards deflection of the ice w is given by

$$D\frac{d^4w}{dx^4} + \rho_w g w = \Delta\rho g h \tag{8}$$

where g is the acceleration due to gravity, x is horizontal distance, $\Delta\rho = \rho_w - \rho$ and h is the local shell thickness (which differs from the background ice shell thickness).

We take the boundary conditions to be $w = d^2w/dx^2 = 0$ at the edge of the refreezing ice (where $x = \pm L$). It may be verified that a suitable solution to eq. (8) is given by

$$w = \frac{h\Delta\rho}{\rho_w}\left[1 - \frac{C\cos kx\cosh kx + S\sin kx\sinh kx}{C^2+S^2}\right] \tag{9}$$

where $C = \cos kL \cosh kL$, $S = \sin kL \sinh kL$ and

$$k = \left(\frac{\rho_w g}{4D}\right)^{1/4}. \tag{10}$$

The quantity k is the inverse of the usual flexural parameter. When $D = 0$, eq. (9) gives the isostatic response, and when $D \to \infty$, $w \to 0$, as required. The symmetry of the solution means that $dw/dx = 0$ at $x = 0$.

Note that this expression does not make any predictions about the elevation of the ice relative to the surrounding (unmelted) material: this elevation contrast depends on the densities of the unmelted and refreezing ice, and is discussed below. Although the expression is Cartesian, it is unlikely to differ except in detail to the equivalent axisymmetric result.

Equation (9) shows that for flexural parameters much less than the domain width, the response of the ice sheet will be similar to an isostatic case, while at large flexural parameters the vertical uplift is reduced. The characteristic distance from the margin over which uplift occurs (Fig. 7c) is determined by the flexural parameter. If T_e increases along with h, which is the likely situation in a re-freezing ice layer, the uplift initially increases (because h is increasing). However, if the flexural parameter becomes comparable to the domain width, the rigidity of the ice begins to dominate and further increases in T_e and h result in reduced uplift. Irrespective of T_e, once the refreezing shell reaches the thickness of the surrounding, unmelted ice, the shape of the topography profile will not change subsequently. In particular, as long as the margin of the refreezing ice remains welded at its original level (see Fig. 7b), a marginal trough will remain irrespective of the shell thickness. Thus, h provides only a lower bound on the present-day shell thickness.

To compare our theoretical model with the observations of an area in which the marginal trough is prominent (Fig. 2), we fix L at the observed trough distance and vary h and T_e simultaneously until the minimum misfit of the model with the observations is obtained. Fig. 8a shows the stacked profile from Fig. 2 together with the minimum misfit profile thus obtained. The best-fit values of h and T_e are 1750 m and 250 m, respectively, and the minimum misfit is 0.32 standard deviations. The present model provides a good fit to the observations; note, however, that inclusion in the observations of profiles 7-9 from Fig. 1 (which do not show a prominent marginal trough) would decrease the goodness of fit. Fig. 8b plots the variation in misfit with T_e and shows that there is a very clearly defined minimum misfit position. Carrying out the same procedure for profile 12 (Fig. 1b) yields values for h and T_e of 850 m and 100 m, respectively, while for profile 13 the (poorly-constrained) values are 400 m and 350 m, respectively. **Fig. 8**

In Fig. 8a the elevation which the surrounding terrain would occupy if it had the same density and thickness as the refreezing ice is shown by the dotted line. This expected elevation exceeds that observed by ≈100 m. This difference could be explained if the refreezing ice were 50 kg m^{-3} less dense than the unmelted ice. Whether such a contrast is likely depends on the ability of the refreezing ice to incorporate contaminants, such as salts, which may be present in unmelted ice (Kargel et al. 2000). The resulting density contrasts are unlikely to exceed 100 kg m^{-3}, so that compositional contrasts alone cannot explain updoming in excess of ≈200 m for shell thicknesses of ≤2 km. Updoming in excess of this amount is observed by Schenk and Pappalardo (2004), implying additional or alternative mechanisms must be operating. An additional contribution could be due to the elevated temperature of the refreezing ice relative to the surroundings, but (as with Section 3), such elevated temperatures would diffuse away with time. Lateral variations in porosity can also generate uplift (Nimmo et al. 2003a), but such variations are typically confined to the top quarter or third of the ice shell, and would have to be very large (30-40%) to explain the observations. Finally, a thicker ice shell would generate the same elevation contrast with smaller lateral density contrasts. However, the data suggest a thin shell at the time of refreezing, and there is no reason to suppose that later shell thickening would preferentially generate density contrasts at the site of existing refrozen regions.

One aspect of the observations which is not fit by the melt-through model is the apparent downwarping towards the margins of the chaos region. Such downwarping has also been observed by Figueredo et al. (2002) at Murias Chaos, and was there attributed to flexure due to surface load emplacement. Although there are hints of surface extrusion at the margins of CH1, we argued in Section 2 that the downwarping observed there may be an artefact. Nor is there any similar downwarping around CH2 (Fig. 1b). Thus, this disagreement between theory and observation is probably not significant.

For Fig. 8a the value of T_e obtained is less than that of the ice thickness. This result is reasonable, since both brittle failure and ductile yielding are likely to occur and will reduce T_e relative to h (e.g. Nimmo et al. 2003b). The local shell thickness h of a few km obtained here is very similar to the estimates of Williams and Greeley (1998) and Carr et al. (1998), and suggests that the melt-through model is at least internally self-consistent. As explained above, the value of h obtained is probably set by the point at which the refreezing material reaches the thickness of the surrounding shell; this local shell thickness is not necessarily the present-day value. Subsequent uniform cooling and thickening of the ice shell would not affect the pre-existing topography. If, however, the shell subsequently began to convect, then newer topography caused by diapirism might be superimposed on the pre-existing, non-diapiric features.

The elastic bending stresses are proportional to d^2w/dx^2 in equation 9. The surface stresses are 4-6 MPa for a Young's modulus of 1 GPa, sufficient to cause fracture. However, these bending stresses decrease to zero at a point half-way through the elastic portion of the ice shell, and are likely to be relieved by ductile creep in the lower portion of the shell. Thus, equation 9 predicts surface failure but does not necessarily imply that the shell will suffer throughgoing fracture.

The model presented here assumes that the ice outside the chaos region is stationary. Whether this is really likely to be the case depends on its rigidity, which may be greater than that of the refreezing ice. The upthrust exerted on the chaos ice will also act on the unmelted ice beyond, and could potentially dome these unmelted regions upwards. This prediction agrees with the observations that in some cases the updomed topography extends beyond the edge of the chaos region (Section 2). On the other hand, the profile in Fig. 8a does not support this prediction, although as discussed above the apparent downwarping is probably not a robust feature.

5 Discussion and Conclusions

This paper has produced simple quantitative models of two suggested chaos formation mechanisms, and tested them against observations, primarily the E15 high resolution images and topography. The principal observations (Section 2) are that chaos regions can consist of elevated, domical areas, often surrounded by an inwards-facing cliff. The domical uplift sometimes extends beyond the edges of the chaos region.

While a $\sim$2 km thick ice shell is possible if Europa's mantle resembles that of Io, it is unclear whether local melt-through events are energetically possible. In Section 4 we show that a simple model of ice refreezing following such a melt-through event can plausibly reproduce several aspects of the observed topography, in particular the cliff-like margin and the domical uplift. The predicted ice shell thicknesses at the time of chaos formation of 0.5-2 km are consistent with previous estimates for chaos regions based on a melt-through assumption. The elastic thicknesses derived (0.1-0.3 km) are also similar to those previously obtained in chaos regions. However, for the low shell thicknesses derived, implausibly large density contrasts are required to explain the observed elevation contrasts of >200 m between background plains and chaos centres. Thus, the refreezing model has difficulty reproducing all the observations.

The hybrid diapir model can reproduce the domical appearance including uplift beyond the edges of the chaos regions. However, for the model to be able to explain lateral chaos block motion and cliff formation, significant melt needs to be generated within about 1-3 km of the surface. Thermal modelling results (Section 3.1) show that generating such melt appears to be impossible for reasonable parameter choices. This conclusion holds even if a relatively thick insulating surface layer and tidal dissipation are included.

For the hybrid diapir model, there appear to be only two ways of generating the required quantities of melt in the near sub-surface. One is to use a very thick ($\delta >$35 km), low-conductivity surface layer. However, such a layer is likely to be only a transient phenomenon, since the increased subsurface temperatures will lead to rapid pore space reduction (Fanale et al. 1990); furthermore, the layer would have a low density and thus provide a barrier to further ascent of the diapir. A slightly more likely explanation is that the diapir model presented here does not fully account for the damage and tidal dissipation generated by a rising diapir (Tobie et al. 2004). We also note that the presence of clathrate hydrates might significantly influence the temperature structure, and provide a possible explanation for the surface degradation and volume loss inferred.

Any future model of chaos formation will have to explain the commonly elevated centres; occurrences of depressed, cliff-like edges; and variably-disrupted interiors of these regions. It seems possible that some kind of diapiric activity which includes surface extrusion of material, leading to marginal downwarping, could potentially explain these observations (c.f. Figueredo et al. 2002).

To demonstrate the plausibility of such a model, we employ the axisymmetric, spreading isoviscous fluid approach of McKenzie et al. (1992). In this model, the total extrusion timescale is set by the cooling time of the fluid drop, which is controlled by its thickness. The rate of lateral flow is controlled by both the fluid thickness and its (constant, Newtonian) viscosity. Equation (21) of McKenzie et al. (1992) may be rewritten to obtain the effective viscosity η of the spreading fluid drop:

$$\eta = \frac{c\rho g h_0^5}{\kappa r_0^2}. \tag{11}$$

Here r_0 and h_0 are the radius and thickness of the fluid drop, κ is the thermal diffusivity and c is a constant (=0.18). From Figs. 1 and 2 we estimate r_0=5 km and h_0=300 m, which gives $\eta = 2 \times 10^{13}$ Pa s. Since the effective viscosity of ice close to its melting point is typically $10^{13} - 10^{15}$ Pa s (Pappalardo et al. 1998), it is apparent that the observed shape could be generated by extrusion of warm ice and thus that the proposed mechanism is at least potentially plausible. Further work, in particular a more detailed treatment of the ice rheology and cooling, will be required to place this hypothesis on a firmer footing.

Acknowledgements

We would like to thank Bob Pappalardo, Patricio Figueredo, Franck Marchis and Vicki Hansen for helpful discussions, and careful reviews by Geoff Collins and an anonymous reviewer. This work funded by NASA-PGG NNG04GE89G.

References

Allison, M.L., Clifford, S.M. 1987. Ice-covered water volcanism on Ganymede. J. Geophys. Res. 92, 7865-7876.

Barnett, D.N., Nimmo, F., McKenzie, D. 2002. Flexure of Venusian lithosphere measured from residual topography and gravity. J. Geophys. Res. 107, doi:10.1029/2000JE001398, 5007.

Billings, S.E., Kattenhorn, S.A. 2002. Determination of ice crust thickness from flanking cracks along ridges on Europa, Lunar Planet. Sci. Conf. XXXIII, 1813.

Buck, L., Chyba, C.F., Goulet, M., Smith, A., Thomas, P. 2002. Persistence of thin ice regions in Europa's ice crust. Geophys. Res. Lett. 29, doi:10.1029/2002GL016171, 2055.

Budd, W.F., Jacka, T.H. 1989. A review of ice rheology for ice-sheet modeling. Cold Reg. Sci. Technol. 16, 107-144. Carlson, R.W., Johnson, R.E., Anderson, M.S. 1999. Sulfuric acid on Europa and the radiolytic sulfur cycle. Science 286, 97-99.

Carr, M.H., et al. 1998. Evidence for a subsurface ocean on Europa. Nature 391, 363-365.

Carslaw, H.S. and J.C. Jaeger. 1959. Conduction of heat in solids (2nd ed). Oxford Univ. Press.

Collins, G.C., Head, J.W., Pappalardo, R.T., Spaun, N.A. 2000. Evaluation of models for the formation of chaotic terrain on Europa. J. Geophys. Res. 105, 1709-1716.

De Pater, I., Marchis, F., Macintosh B.A., Roe, H.G., Le Mignant, D., Graham, J.R., Davies, A.G. 2004. Keck AO observations of Io in and out of eclipse. Icarus 169, 250-263.

Fanale, F.P., Salvail, J.R., Matson, D.L., Brown, R.H. 1990. The effect of volume phase-changes, mass-transport, sunlight penetration and densification on the thermal regime of icy regoliths, Icarus 88, 193-204.

Fanale, F.P., Li, Y.-H., De Carlo, E., Farley, C., Sharma, S.K., Horton, K., Granahan, J.C. 2001. An experimental investigation of Europa's ocean composition independent of Galileo orbital remote sensing. J. Geophys. Res. 106, 14595-14600.

Figueredo, P., Chuang, F.C., Rathbun, J., Kirk, R.L., Greeley, R. 2002. Geology and origin of Europa's "Mitten" feature (Murias Chaos), J. Geophys. Res. 107, doi:10.1029/2001JE001591, 5026.

Gaidos, E., Nimmo, F. 2000. Tectonics and water on Europa. Nature 405, 637.

Giese, B., Oberst, J., Roatsch, T., Neukum, G., Head, J.W., Pappalardo, R.T. 1998. The local topography of Uruk Sulcus and Galileo Regio obtained from stereo images. Icarus 135, 303-316.

Goodman, J.C., Collins, G.C., Marshall, J., Pierrehumbert, R.T. 2004. Hydrothermal plume dynamics on Europa: Implications for chaos formation. J. Geophys. Res. 109, doi:10.1029/2003JE002073, E03008.

Greeley, R., et al. 1998. Europa: Initial Galileo geological observations. Icarus 135, 4-24.

Greenberg, R., Hoppa, G., Tufts, R., Geissler, P., Riley, J., Kadel, S. 1999. Chaos on Europa. Icarus 141, 263-286.

Greenberg, R., Geissler, P., Hoppa, G.V., Tufts, B.R. 2002. Tidal-tectonic processes and their implications for the character of Europa's ice crust. Rev. Geophys. 40, 1-33.

Greenberg, R., Leake, M.A., Hoppa, G.V., Tufts, B.R. 2003. Pits and uplifts on Europa. Icarus 161, 102-126.

Head, J.W., Pappalardo, R.T. 1999. Brine mobilization during lithospheric heating on Europa: Implications for formation of chaos terrain, lenticula texture, and color variations. J. Geophys. Res. 104, 27143-27155.

Hurford, T.A., Preblich, B., Beyer, R.A., Greenberg, R. 2004. Flexure of Europa's lithosphere due to ridge-loading. Lunar Planet. Sci. Conf. XXXV, 1831.

Kadel, S.D., Chuang, F.C., Greeley, R., Moore, J.M. 2000. Geological history of the Tyre region of Europa: A regional perspective on Europan surface features and ice thickness. J. Geophys. Res. 105, 22657-22669.

Kargel, J.S., Kaye, J.Z., Head, J.W., Marion, G.M., Sassen, R., Crowley, J.K., Ballesteros, O.P., Grant, S.A., Hogenboom, D.L. 2000. Europa's crust and ocean: Origin, composition and the prospects for life. Icarus 148, 226-265.

Mader, H.M. 1992. Observations of the water-vein system in polycrystalline ice. J. Glaciol. 38, 333-347.

McKenzie, D. 1989. Some remarks on the movement of small melt fractions in the mantle. Earth Planet. Sci. Lett. 95, 53-72.

McKenzie, D., Ford, P.G., Liu, F., Pettengill, G.H. 1992. Pancake-like domes on Venus. J. Geophys. Res. 97, 15967-15975.

McKenzie, D., Nimmo, F. 1999. The generation of Martian floods by melting permafrost above dykes. Nature 397, 231-233.

McKinnon, W.B. 1999. Convective instability in Europa's floating ice shell. Geophys. Res. Lett. 26, 951-954.

Melosh, H.J., Ekholm, A.G., Showman, A.P., Lorenz, R.D. 2004. The temperature of Europa's subsurface water ocean. Icarus 168, 498-502.

Murray, C.D., Dermott, S.F. 1999. Solar system dynamics. Cambridge Univ. Press.

Nimmo, F., 2004. Non-Newtonian topographic relaxation on Europa. Icarus 168, 205-208.

Nimmo, F., Manga, M. 2002. Causes, characteristics and consequences of convective diapirism on Europa. Geophys. Res. Lett. 29, doi:10.1029/2002GL015754, 2109.

Nimmo, F., Pappalardo, R.T., Giese, B. 2003a. On the origins of band topography, Europa. Icarus 166, 21-32.

Nimmo, F., Giese, B., Pappalardo, R.T. 2003b. Estimates of Europa's ice shell thickness from elastically-supported topography. Geophys. Res. Lett. 30, doi:10.1029/2002GL016660, 1233.

O'Brien, D.P., Geissler, P., Greenberg, R. 2002. A melt-through model for chaos formation on

Europa. Icarus 156, 152-161.

Pappalardo, R.T. et al. 1998. Geological evidence for solid-state convection in Europa's ice shell. Nature 391, 365-368.

Pappalardo, R.T., Barr, A.C. 2004. The origin of domes on Europa: The role of thermally induced compositional buoyancy. Geophys. Res. Lett. 31, doi:10.1029/2003GL019202, L01701.

Pappalardo, R.T. et al. 1999. Does Europa have a surface ocean? Evaluation of the geological evidence. J. Geophys. Res. 104, 24015-24055.

Peale, S.J., Cassen, P., Reynolds, R.T. 1979. Melting of Io by tidal dissipation. Science 203, 892-894.

Prieto-Ballesteros, O., Kargel, J.S., Fernandex-Sampedro, M. , Hogenboom, D.L. 2004. Evaluation of the possible presence of CO_2 clathrates in Europa's icy shell or seafloor. Lunar Planet. Sci. Conf. XXXV, 1748.

Prieto-Ballesteros, O., Kargel, J.S. 2004. Thermal state and complex geology of a heterogeneous salty crust of Jupiter's satellite, Europa. Icarus in press.

Rathbun, J.A., Musser, G.S., Squyres, S.W. 1998. Ice diapirs on Europa: Implications for liquid water. Geophys. Res. Lett. 25, 4157-4160.

Ross, R.G., Kargel, J.S. 1998. Thermal conductivity of solar system ices, with special reference to Martian polar caps. in B. Schmitt et al. (eds.), Solar System Ices, Kluwer Academic, pp. 33-62.

Schenk, P.M., Pappalardo, R.T. 2004. Topographic variations in chaos on Europa: Implications for diapiric formation. Geophys. Res. Lett. 31, doi:10.1029/2004GL019978, L16703, 2004.

Showman, A.P., Han, L.J. 2004. Numerical simulations of convection in Europa's ice shell: Implications for surface features. J. Geophys. Res. 109, doi:10.1029/2003JE002103, E01010.

Sotin, C., Head, J.W., Tobie, G. 2002. Europa: tidal heating of upwelling thermal plumes and the origin of lenticulae and chaos melting. Geophys. Res. Lett. 29, doi:10.1029/2001GL013844, 1233.

Spaun, N.A., Head, J.W., Collins, G.C., Prockter, L.M., Pappalardo, R.T. 1998. Conamara Chaos Region, Europa: Reconstruction of mobile polygonal ice blocks. Geophys. Res. Lett. 25, 4277-4280.

Spaun, N.A., Head, J.W., Pappalardo, R.T. 1999. Chaos and lenticulae on Europa: Structure, morphology and comparative analysis. Lunar Planet. Sci. Conf. XXX, 1276.

Spencer, J.R., Tamppari, L.K., Martin, T.Z., Travis, L.D. 1999. Temperatures on Europa from Galileo photopolarimeter-radiometer: Nighttime thermal anomalies. Science 284, 1514-1516.

Squyres, S.W., Reynolds, R.T., Cassen, P.M., Peale, S.J. 1983. Liquid water and active resurfacing on Europa. Nature 301, 225-226.

Thomson, R.E., Delaney, J.R. 2001. Evidence for a weakly stratified Europan ocean sustained by seafloor heat flux. J. Geophys. Res. 106, 12355-12365.

Tobie, G., Choblet, G., Sotin, C. 2003. Tidally heated convection: Constraints on Europa's ice shell thickness. J. Geophys. Res. 108, doi:10.1029/2003JE002099, 5124.

Tobie, G., Choblet, G., Lunine, J., Sotin, C. 2004. Interaction between the convective sublayer and the cold fractured surface of Europa's ice shell. Workshop on Europa's icy shell, LPI contrib. no. 1195, 89-90.

Turcotte, D.L. and Schubert, G. 2002. Geodynamics. Cambridge University Press.

Veeder, G.J., Matson, D.L., Johnson, T.V., Blaney, D.L., Goguen, J.D. 1994. Io's heat flow from infrared radiometry: 1983-1993. J. Geophys. Res. 99, 17095-17162.

Wang, H., Stevenson, D.J. 2000. Convection and internal meting of Europa's ice shell. Lunar Planet. Sci. Conf. XXXI, 1293.

Williams, K.K., Greeley, R. 1998. Estimates of ice thickness in the Conamara Chaos region of Europa. Geophys. Res. Lett. 25, 4273-4276.

Zolotov, M.Y., Shock, E.L. 2001. Composition and stability of salts on the surface of Europa and their oceanic origin. J. Geophys. Res. 106, 32815-32827.

Appendix

Here we describe the numerical approach involved in our calculations of diapir-induced melting (see Fig. 4). Further details may be found in McKenzie and Nimmo (1999).

At each grid-point (i, j), the upwards, downwards and lateral heat fluxes F_N,F_S,F_E and F_W are calculated using

$$F_N \Delta z = k_{j-\frac{1}{2}}[T(i,j) - T(i,j-1)] \tag{12}$$

and similar expressions, where k_j is the (vertically-varying) thermal conductivity, $T(i, j)$ is the temperature at grid point (i, j), j increases with depth and the vertical grid spacing Δz equals the horizontal grid spacing Δx. Note that a positive value denotes an outwards heat flow.

The total change in heat per unit length of a grid point ΔH is given by

$$\Delta H(i,j) = -\Delta t \Delta x(F_N + F_E + F_S + F_W - H_{int}\Delta x) \tag{13}$$

where Δt is the time step and H_{int} is the internal heat generation rate in W m^{-3}.

For ice which does not reach its melting temperature, the total temperature change $\Delta T(i, j)$ is given by

$$\Delta T(i,j) = \Delta H(i,j)/(\rho C_p \Delta x^2) \tag{14}$$

where ρ and C_p are the density and specific heat capacity of the material, respectively.

Melting is assumed to occur in a linear fashion over a range $T_m - \Delta T_m/2$, $T_m + \Delta T_m/2$. If $\Delta T(i, j)$ is such that the solidus is exceeded, then the change in temperature over the melting interval is calculated using equation (14) except that C_p is replaced by $C_p + L/\Delta T_m$, where L is the latent heat of melting.

The initial temperature of the diapir is cosine-tapered to the background value over the top and bottom 15% of the block, and laterally over the outer 30%, to mimic the cooling of the diapir as it rises through the ice shell. For the nominal case (Fig. 4), removing the tapers changes the shallowest depth at which melt is produced by less than 2%. Temperatures are updated each time step by using equation (14). The boundary conditions are reflecting at the side boundaries, fixed at the top and bottom.

A grid spacing of 0.125 km was used in both the x and z directions, and a fixed timestep of 10^8 s was adopted. Increasing the spatial or temporal resolution further had minor (<10%) effects on the results. The extra energy delivered to the system by the sill was typically conserved to within a few percent during model runs. As an additional check on the accuracy of the results, it was verified that the analytical solution of Carslaw and Jaeger (1959, section 2.2 eq. 3) was reproduced when the thermal gradient was zero and no melting occurred.

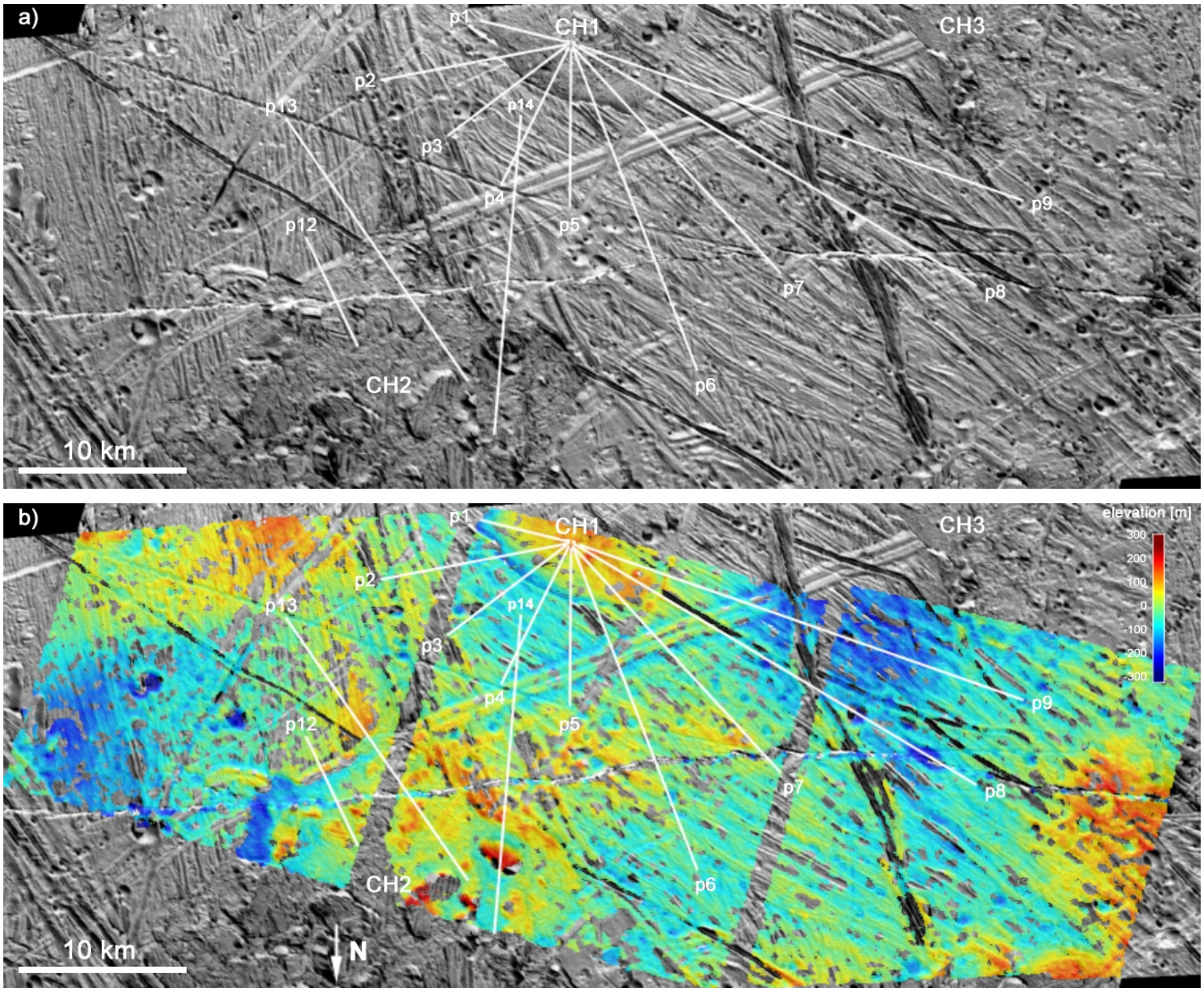

Figure 1: a) Galileo high resolution image of area SE of Tyre impact crater. Image resolution 30 m/pix, taken on 31 May 1998, centred at approximately 31°N, 142°W. Profiles shown are used in generating Fig 2. Note that north is to the bottom of the image; illumination from the top of the image. b) Stereo topography of same region, horizontal resolution 200-400 m, vertical accuracy 10 m.

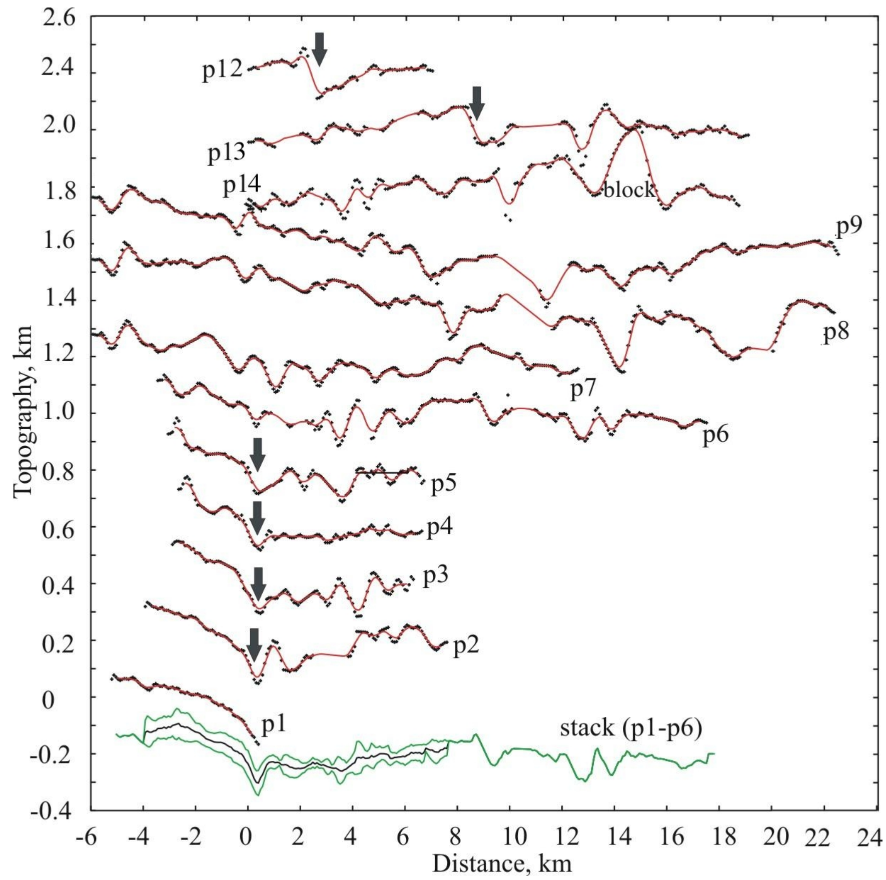

Figure 2: Topographic profiles across E15 area. Location of profiles shown in Fig 1. Successive profiles are offset vertically by 0.2 km and the mean elevation was removed. Black crosses are the data, interpolated to 80 m spacing; red lines are filtered using a 7 point moving average. Arrows denote cliff-like margin of chaos regions (see text). Profiles p1-p6 are aligned on the steepest point of the filtered data within 6 km of the origin. The bottom profile is the result of stacking the observations, with the green lines showing ± one standard deviation (s.d.).

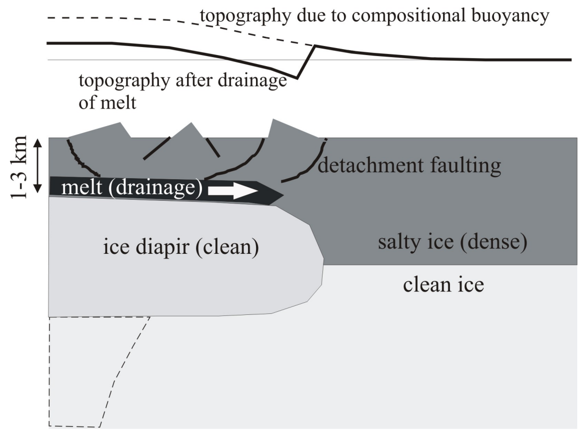

Figure 3: Schematic of model for chaos formation by diapirism, after Collins et al. (2000). Warm diapir ascends into salty ice and causes melting. The melt zone may allow detachment faulting and surface block movement to occur. If the melt drains laterally and/or downwards it will produce subsidence at the surface. The compositional buoyancy of the diapir causes topographic uplift over a wider area than the subsidence, due to the rigidity of the overlying ice.

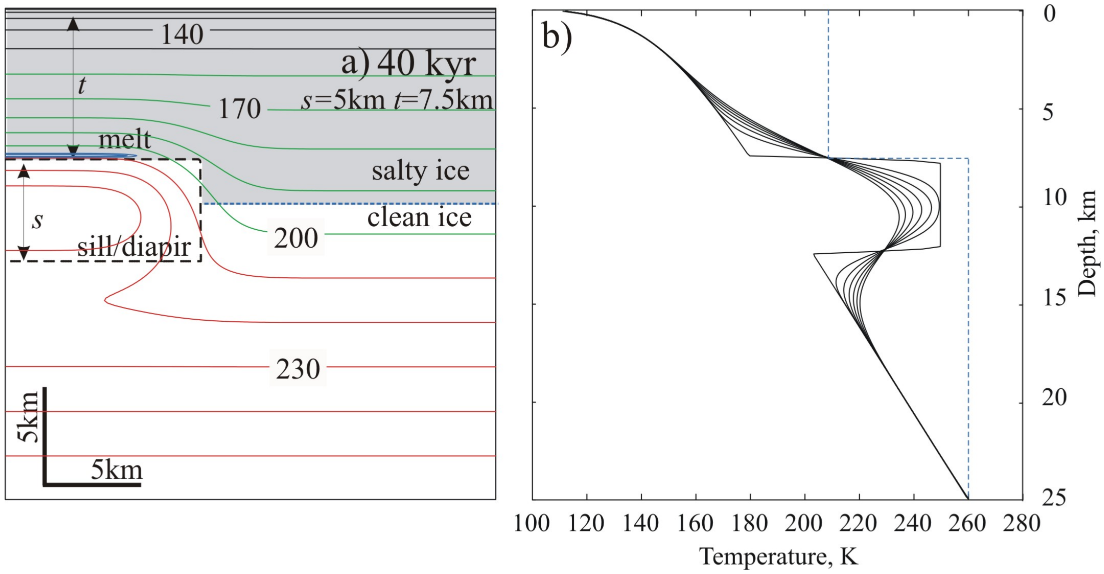

Figure 4: a) Typical outcome of melting models described in Section 3.1, plotted at the instant of maximum melt production (40 kyr). Solid lines are temperature contours (in K). Initial diapir location denoted by dashed lines; initial diapir temperature 250 K. Light shaded area denotes location of salty ice (melting temperature 210 K). Thin dark shaded area above the diapir depicts points at which partial melt generation occurs. The mean thickness of the meltwater lens overlying the diapir is 30 m. The conductivity length-scale δ was 3 km. b) Evolution of vertical temperature profile through centre of diapir with time. Curvature of near-surface profile is due to variable thermal conductivity. Dotted line denotes melting curve of ice. Profiles are plotted at intervals of 8 kyr.

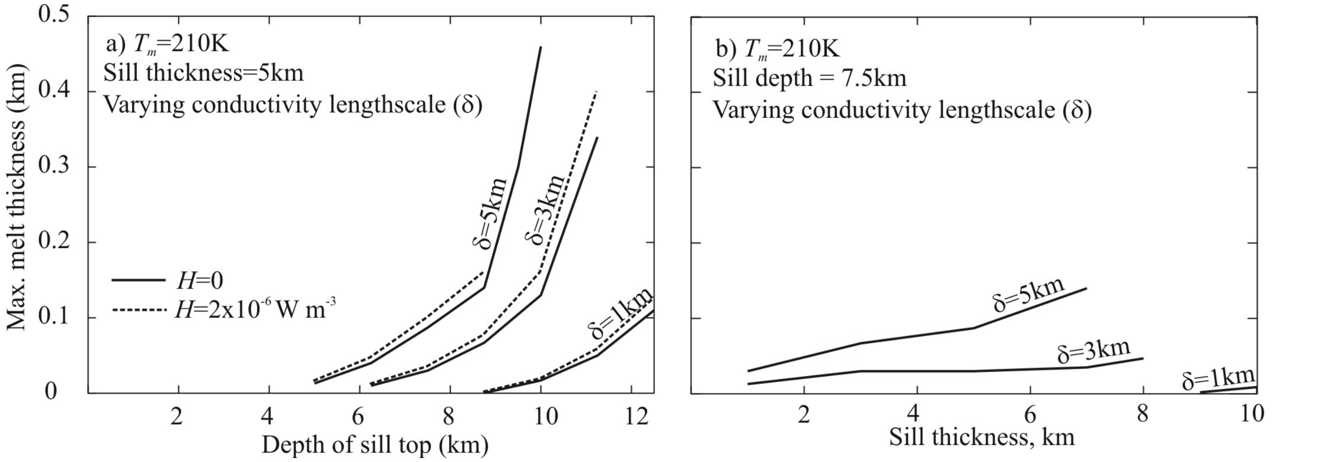

Figure 5: a) Variation of maximum melt thickness as a function of depth to top of diapir and conductivity length-scale δ for a shell of thickness 25 km. Solid lines are for no tidal dissipation within diapir (H=0); dashed lines are for H=2×10^{-6} W m^{-3}. T_m is ice melting temperature. The top of melting zone is never more than 1 km above the top of the sill. b) Variation in melt thickness as a function of sill thickness and δ (depth to top of sill 7.5 km).

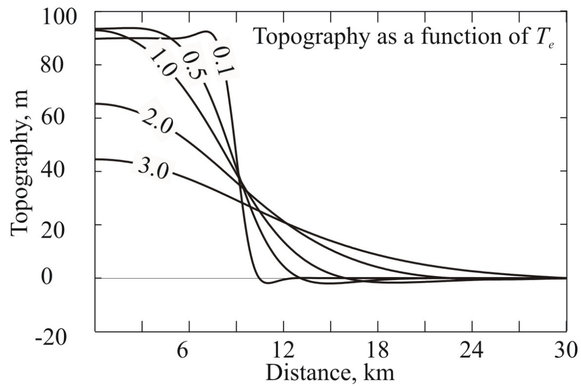

Figure 6: Variation in surface topography with elastic thickness T_e for a fixed axisymmetric subsurface load, calculated using the method described in the text. Load width is 10 km, cosine tapered over the outer 20%, and generates 90 m uplift in isostatic case. Young's modulus is 1 GPa, Poisson's ratio 0.3, acceleration due to gravity 1.3 m s^{-2}, ice density 900 kg m^{-3}.

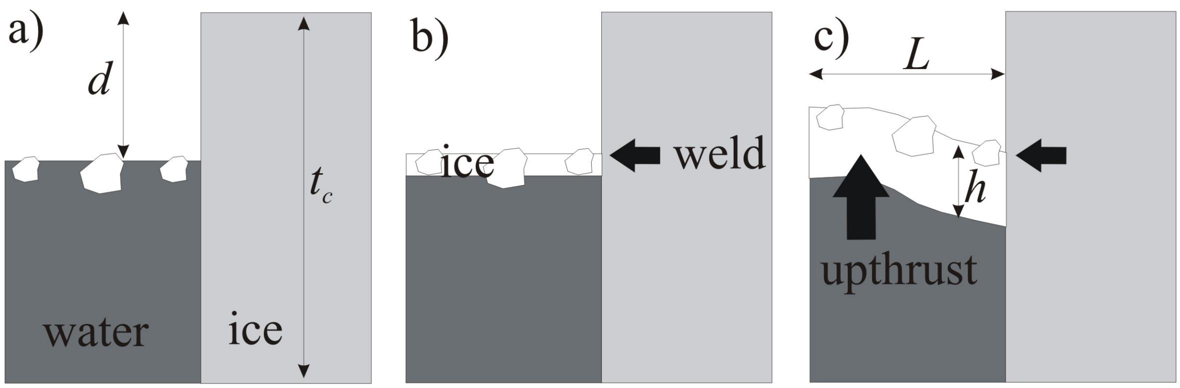

Figure 7: Schematic showing development of chaos topography following "melt-through" event. a) Melt-through leads to water (and remanent ice-blocks) at level d beneath the unmelted ice. b) Refreezing ice is assumed to remain welded at initial level. c) Thickening of ice results in upthrust and consequent up-doming of ice away from the edge.

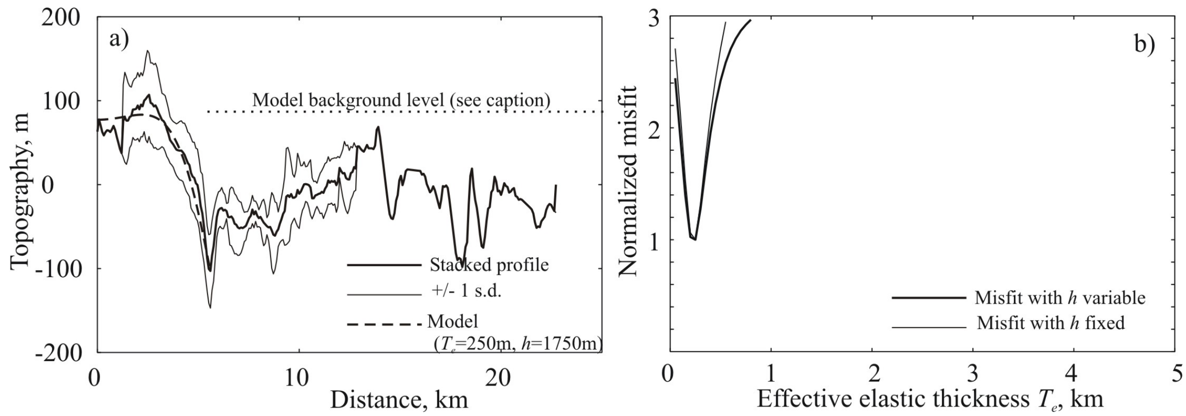

Figure 8: Bold line is stacked topographic profile of E15 area, replotted from Fig 2. Thin lines are ±1 standard deviation (s.d.). Dashed line is best-fit model assuming melt-through (eq. 9). Best-fit ice thickness h is 1750 m and T_e =250 m. b) Misfit, normalized to the minimum value of 0.32 standard deviations, as a function of T_e. Misfit is calculated over the domain indicated by the dashed line in a). Bold line plots misfit when h is allowed to vary for each value of T_e; thin line plots misfit when h is fixed at 1750 m. Dotted line indicates elevation of background terrain assuming same density and thickness as the re-freezing ice (see text).